Int. J. Electrochem. Sci., 14 **(2019)** 8805 – 8818, doi: 10.20964/2019.09.21

International Journal of
ELECTROCHEMICAL
SCIENCE
www.electrochemsci.org

Production and Characterization of Chromium Oxide (Cr_2O_3) via a Facile Combination of Electrooxidation and Calcination

Sen Tian[1,2,3], Xuemei Ye[1,2,3], Yaping Dong[1,2,], Wu Li[1], Bo Zhang[1,2], Bo Li[1,2], Haitao Feng[1,2,*]*

[1] Key Laboratory of Comprehensive and Highly Efficient Utilization of Salt Lake Resources, Qinghai Institutes of Salt Lakes, Chinese Academy of Sciences, Xining, 810008, China
[2] Qinghai Engineering and Technology Research Center of Comprehensive Utilization of Salt Lake Resources, Xining, 810008, China
[3] University of Chinese Academy of Sciences, Beijing, 100049, China
[*]E-mail: fenght@isl.ac.cn (H. Feng), dyp811@126.com (Y. Dong).

Received: 24 April 2019 / *Accepted:* 26 June 2019 / *Published:* 31 July 2019

To synthesize Cr_2O_3 from ferrochromium, the electrolysis of ferrochromium in an electrolyzing cell and the properties of Cr_2O_3 prepared by thermal decomposition of $(NH_4)_2CrO_4$ were studied. Experimental results showed that with a 1:5 molar ratio of $NH_3{\cdot}H_2O$:$2CrO_4^{2-}$ and current density of 140 A/m^2 at room temperature, Cr and Fe can be completely separated by solid-liquid separation, and $(NH_4)_2CrO_4$ can be obtained. The optimized current efficiency was 62%. The four-step thermal decomposition process of $(NH_4)_2CrO_4$ was analyzed by TG-DTA. The XRD and FTIR results proved that crystalline Cr_2O_3 with a fine particle size was obtained. Spherical Cr_2O_3 with a particle size of 71~216 nm and a specific surface area of 4~38 m^2/g was confirmed by SEM and BET. UV-Vis results proved that Cr_2O_3 presented bright green (L*=34.78~49.97, a*=0.91~-14.73, and b*=6.08~17.92), and the forbidden band width was 1.91~2.25 eV. The purity of Cr_2O_3 was over 99%.

Keywords: Ferrochromium, Electrooxidation, $(NH_4)_2CrO_4$, Thermal decomposition, Cr_2O_3

1. INTRODUCTION

Cr_2O_3 is an important inorganic material with extensive applications, including as catalysts [1], electrode materials for supercapacitors [2], hydrogen sorption materials [3], pigments [4] and solar absorbers [5]. Generally, common processes for the production of Cr_2O_3 used by most manufacturers involve the reduction of alkali metal dichromate ($Na_2Cr_2O_7$ or $K_2Cr_2O_7$) [6] or the thermal decomposition of CrO_3 [7]. Two front-end products of Cr_2O_3 are hexavalent chromium compounds, the traditional production process of which presently includes three steps: roasting of chromite ore, water leaching, and multistage evaporation and crystallization. However, the waste of raw materials and energy

in the above process is generally quite high [8]. Furthermore, a great quantity of Cr(VI)-containing toxic wastes released from chromate plants threaten the environment and human health [9]. Recently, several preparation processes for Cr_2O_3 have been investigated, such as sonochemical [10], sol-gel [11], solvothermal [12], microwave refluxing [13] and precipitation methods [14]. These methods have achieved the preparation of Cr_2O_3 with special properties. However, these methods inevitably involve the hexavalent chromium compound preparation method. Furthermore, these methods are difficult so that it is hard to achieve large-scale manufacturing. The fundamental problem in the production of Cr_2O_3 is the preparation of hexavalent chromium compounds. Therefore, it is important to study the synthesis of Cr_2O_3 from the source using a green and efficient method.

The electrochemical method is a green and efficient preparation method. Although the electrochemical method has been widely used in industrial production, few applications focus on Cr_2O_3. The electrochemical method has attractive features for industrial production, including high atom efficiency, and is used for the transformation of matter through electron transfer [15], is environmentally friendly through its use of electric energy [16], has a high energy efficiency compared to chemical processes [17], and causes less pollution by controlling the electrode potential [16]. Initially, electrochemical methods were used in the electrosynthesis of dichromate or chromic anhydride from chromate. However, the valence state of Cr does not change. For the ferrochromium electrooxidation process, hexavalent chromium compounds can be obtained directly from a zero valence by one-step electrolysis, which is unprecedented in chromate production. Compared to the processing time of a traditional production process of hexavalent chromium compounds, one-step electrolysis is a rapid process. The separation of Cr and Fe can be realized by simple solid-liquid separation. The use of an electrochemical method for chromate production should completely change the production of chromium and its compounds.

In this paper, a green and efficient approach that involves a combined electrooxidation and calcination method is proposed to synthesize Cr_2O_3 using ferrochromium and aqueous ammonia as the materials. This work was intended to reform the production of chromium from the source to achieve clean production of Cr_2O_3. In the electrooxidation stage, the effect of current density, molar ratio and temperature on the current efficiency was discussed. In the thermal decomposition stage, the effects of temperature on the crystallinity, morphology, particle size, specific surface area, color and forbidden band width of the synthesized chromium oxide were studied.

2. EXPERIMENTAL

2.1. Materials

Analytical reagent grade $(NH_4)_2CrO_4$ (Shanghai Aladdin Biochemical Science and Technology Co., Ltd., China) and $NH_3 \cdot H_2O$ (Gansu Silver ring chemical industry Co., Ltd., China) were used. The electrolytic tank was constructed in the laboratory with a titanium frame anode and two nickel cathode plates. The ferrochromium composition is shown in Table 1.

Table 1. Composition of ferrochromium, $(NH_4)_2CrO_4$ and Cr_2O_3.

Compound (%)	Cr	Fe	Si	V	P	Others
ferrochromium	59.52	32.83	3.97	0.22	0.18	3.25
Compound (%)	Cr_2O_3	Fe_2O_3	SiO_2	V_2O_5	P_2O_5	Others
$(NH_4)_2CrO_4$	99.41	0.01	0	0	0.18	0.40
Cr_2O_3	99.51	0.02	0	0	0.26	0.21

2.2. Preparation

Fig. 1 shows the preparation route for Cr_2O_3. The ferrochromium particles were loaded into an anode frame with the cathode plates placed on both sides of the anode. Then, $NH_3 \cdot H_2O$ and $(NH_4)_2CrO_4$ were mixed and added into the electrolytic tank. A stable current was maintained for 6 hours and then the power supply was turned off. The electrolyte and precipitation were separated by filtration. The precursor was obtained by crystallization of the electrolyte in the next step. Finally, a series of products was prepared by high-temperature calcination.

The current efficiency (η) was calculated by analyzing the content of Cr(VI) in the filtrate and eluate. The current efficiency (η) was calculated by Eq. (1):

$$\eta = \frac{n(m_2 - m_1)}{MIt} F \qquad (1)$$

where η is the current efficiency; m_1 and m_2 (g) are the quality of $(NH_4)_2CrO_4$ at the beginning and end of electrolysis, respectively; F (96485C·mol^{-1}) is the Faraday constant; I (A) is the current; M is the relative atomic mass of $(NH_4)_2CrO_4$; t (s) is the electrolysis time; and n is the electron transfer number.

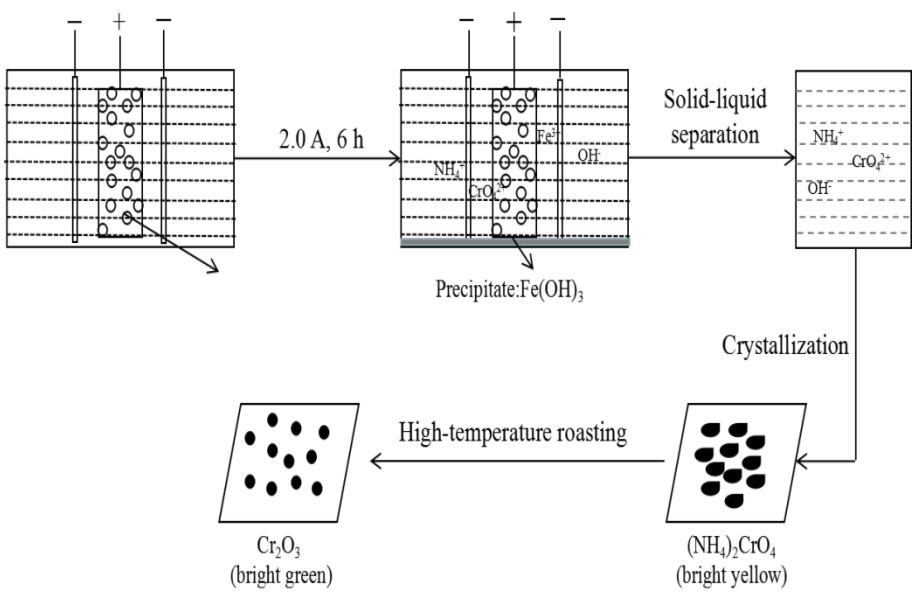

Figure 1. Preparation route of chromium oxide.

2.3. Characterization

Thermogravimetric-differential thermal analysis (TG-DTA) was performed (SDT Q600, TA Instruments Corporation, USA). X-ray diffraction (XRD) patterns of precursors and products were recorded (X′pert Pro, PANalytical, Netherlands). The specific surface area was calculated with the Brunauer-Emmett-Teller (BET) method. Scanning electron microscopy (SEM) was used to determine the morphology and particle size (JSM6360LV/INCA, Electron Company, Japan). Fourier transform infrared (FTIR) spectroscopy was completed (Nexus, Thermo Nicollet, America). The ultraviolet visible diffuse reflectance (UV-vis) spectrum was recorded with a UV-VIS-NIR spectrophotometer (UV-3600 Plus, Shimadzu, Japan). The color performance data were reported by the CIE-L*a*b* colorimetric system. The L* denotes the degree of lightness (L=100) and darkness (L=0) of the color; the a* denotes the degree of the red (+a*) and green (-a*) of the color; the b* denotes the degree of the yellow (+b*) and blue (-b*) of the color.

3. RESULTS AND DISCUSSION

The key step of the process is the synthesis of $(NH_4)_2CrO_4$ via electrooxidation. The rest only needs to be calcined at a high temperature to produce Cr_2O_3. Therefore, the factors affecting the current efficiency were studied to determine the best electrooxidation conditions.

During the electrooxidation process, the anode Cr and Fe lose electrons to CrO_4^{2-} and $Fe(OH)_3$, respectively, while the cathode H_2O is converted to H_2 [18]. Therefore, Cr and Fe become separated. The related reaction equations are as follows:

Anode reaction: $Cr - 6e + 4H_2O \rightarrow CrO_4^{2-} + 8H^+$ (2)

$2Fe - 6e + 4H_2O \rightarrow 2Fe(OH)_3 \downarrow + 6H^+$ (3)

Cathodic reaction: $6H_2O + 6e \rightarrow 3H_2 \uparrow + 6OH^-$ (4)

Total reaction: $2Fe + Cr + 2NH_4OH + 8H_2O \rightarrow (NH_4)_2CrO_4 + 2Fe(OH)_3 \downarrow + 6H_2 \uparrow$ (5)

Cr_2O_3 is therefore obtained by calcination from $(NH_4)_2CrO_4$. The thermal decomposition process is expressed as in Eq. (6):

$2(NH_4)_2CrO_4 \rightarrow 2NH_3 \uparrow + N_2 \uparrow + Cr_2O_3 + 5H_2O$ (6)

3.1. Electrooxidation experiment

3.1.1. Influence of $NH_3 \cdot H_2O$:$2CrO_4^{2-}$ mole ratio

The influence of the $NH_3 \cdot H_2O$:$2CrO_4^{2-}$ ratio on the current efficiency is shown in Fig. 2. The η increased first and then decreased with the change in concentration. Because $NH_3 \cdot H_2O$ and $(NH_4)_2CrO_4$ can be regarded as a pair of pH buffers, the change in the pH had little effect on the current efficiency. Initially, the concentration of $NH_3 \cdot H_2O$ was high, and the conductivity of the solution was low. When the mole ratio changed from 1:20 to 1:5, the conductive particles of the solution increased with the addition of $(NH_4)_2CrO_4$ so that the conductivity of the solution increased. Therefore, the current

efficiency improved. There was little $NH_3 \cdot H_2O$ in the solution with the molar ratio changing to 1:5. At this time, the concentration of $NH_3 \cdot H_2O$ was low, which was the control step of the whole process. When the mole ratio changed from 1:5 to 1:1, a decrease in the ammonia concentration led to an increase in the cell voltage, which caused the side reactions to increase. Thus, the current efficiency gradually decreased.

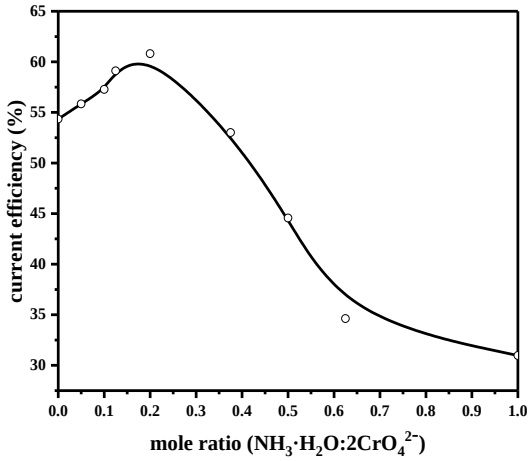

Figure 2. Influence of different $NH_3 \cdot H_2O$:$2CrO_4^{2-}$ mole ratios on the current efficiency at a current density of 133 A/m^2 and room temperature.

3.1.2. Influence of current density

Fig. 3 shows that the current efficiency varied with the current density. The current efficiency increased at the beginning and decreased later with increasing current density. The value of η reached 62% at 140 A/m^2. As the current density was initially low, the voltage for a side reaction was not reached, and electrode polarization was difficult to achieve; thus; the current efficiency was only 56%.

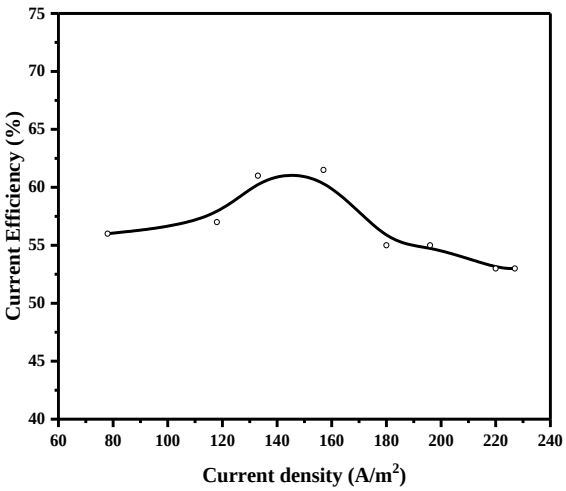

Figure 3. Influence of different current densities on the current efficiency at $NH_3 \cdot H_2O$:$2CrO_4^{2-}$ mole ratios of 1:5 and room temperature.

An increase in the current density increased the electron transfer speed, polarization and reaction rate. Therefore, the current efficiency increased with increasing current density. The moment the cell voltage increased to a certain extent and the current density reached 140 A/m^2, the side reaction began to occur. The higher the current density, the higher the cell voltage and the more side reactions there were. Therefore, the current efficiency decreased.

3.1.3. Influence of temperature

The influence of the temperature on the current efficiency is shown in Fig. 4. The results showed that the current efficiency decreased slightly, accompanied by an increase in the temperature, and η was not greater than 57%. Theoretically, an increase in the temperature caused the electrolyte flow, diffusion speed, ionic activity and exchange rate of the solid-liquid interface to increase, which improved the current efficiency. An increase in the temperature increased electrolyte volatilization, which reduced the amount of $NH_3 \cdot H_2O$ used for the reaction. A decrease in the reaction rate followed a decrease in $NH_3 \cdot H_2O$ per unit area on the anode interface, which caused a decrease in the current efficiency. Therefore, the suitable electrolysis temperature was room temperature.

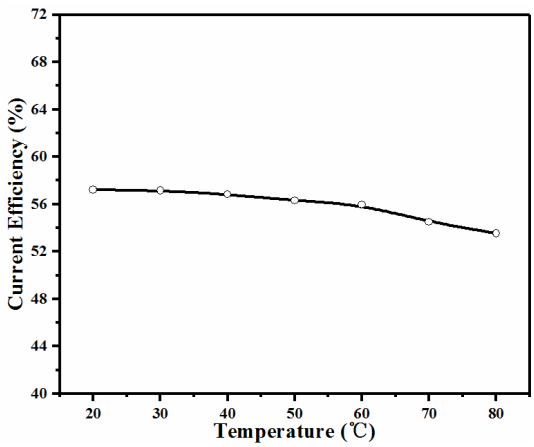

Figure 4. Influence of different temperatures on the current efficiency at the condition of $NH_3 \cdot H_2O$:$2CrO_4^{2-}$ mole ratio 1:5 and at current density 140 A/m^2.

In summary, the optimum η was 62%. Combined with the electrooxidation results and Table 1, the ω_{Cr} of ferrochromium was 59.516% and the η was 62%, which illustrated that highly efficient utilization of ferrochromium was achieved. Therefore, the electrooxidation process demonstrated a green and efficient production process of Cr from the source.

3.2. Precursor performance

The XRD results shown in Fig. 5 proved that the precursor was $(NH_4)_2CrO_4$. Obvious differences in the color of $(NH_4)_2CrO_4$ were observed. The color of the standard was dark-yellow, but the color of

the sample was bright-yellow. This color difference was due to the preferred orientation of the crystal growth due to special crystallization methods. The crystal growth planes in the standard were (3 1 0) oriented, while the crystal growth planes in the sample were (-3 1 1) oriented. The composition of the $(NH_4)_2CrO_4$ is shown in Table 2. The results showed that the purity of the precursor was greater than 99%. Si and V, which are often contained in chromate, usually make the products perform worse [19, 20]. According to Table 1, Si and V were not introduced by electrooxidation. In an aqueous ammonia system, Si and V react with ammonium and precipitate. The Fe content was at the ppm level, which illustrated that the Cr and Fe had been separated. Therefore, a fine precursor was obtained.

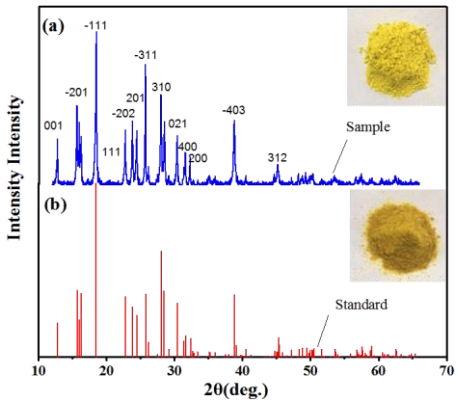

Figure 5. XRD patterns of (a) $(NH_4)_2CrO_4$ sample and (b) $(NH_4)_2CrO_4$ standard.

3.3. Characterization of Cr_2O_3

3.3.1. TG-DTA analysis

The thermogravimetry analysis of $(NH_4)_2CrO_4$ is shown in Fig. 6. There were four obvious exothermic peaks on the DTA curve, which showed that the $(NH_4)_2CrO_4$ decomposed in four steps. According to the measurement, the three intermediate products were $(NH_4)_2Cr_2O_7$, CrO_3 and CrO_2 [21]. Due to the release of NH_3 or N_2 in the first two steps [22], the reaction released a substantial amount of heat. After that, the sample transformed into an oxide with improved stability and released less heat than during the initial stage. The results revealed that the thermal decomposition process of $(NH_4)_2CrO_4$ was followed by the reduction of $Cr^{6+}\rightarrow Cr^{4+}\rightarrow Cr^{3+}$.

The TG curve illustrated that the weight loss reached 51% from 20 to 444 °C and then remained constant. The above results illustrated that the majority of the weight loss seemed to occur below 444 °C. Therefore, we speculated that $(NH_4)_2CrO_4$ would be completely converted into Cr_2O_3 above 444 °C. In this paper, 450 °C, 550 °C, 650 °C, 750 °C, 850 °C, 950 °C, 105 °C and 1150 °C were chosen as the calcination temperatures to study the effect of temperature on the Cr_2O_3 performance.

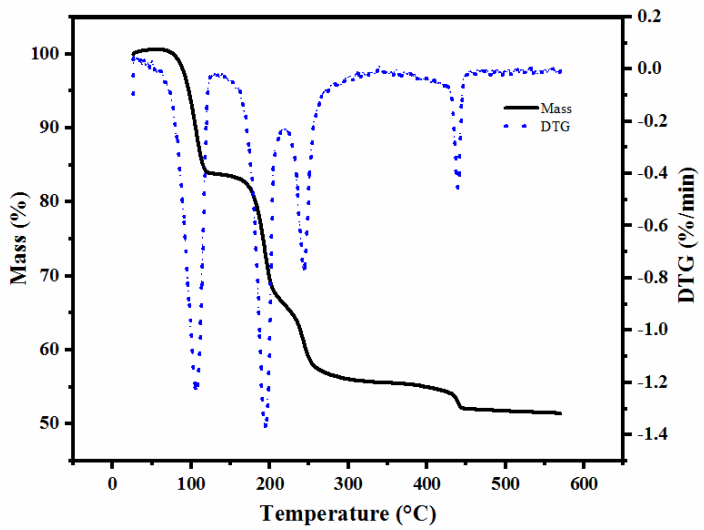

Figure 6. TG-DTA curve of thermal decomposition of $(NH_4)_2CrO_4$.

3.3.2. XRD analysis

Fig. 7 shows the XRD patterns and the crystallite sizes of the samples. The major XRD peaks of the products, including (0 1 2), (1 0 4), (1 1 0), (1 1 3), (0 2 4), (1 1 6), (2 1 4), (3 0 0), (1 1 9) and (2 2 0), can be indexed to α-Cr_2O_3, which is in agreement with the standard value for the Cr_2O_3 phase (JCPDS card No. 1308-38-9, hexagonal close-packed, a=4.958 Å, and c=13.59 Å). The XRD results agreed with the FTIR results (Fig. 9), which contained the characteristic bands for the Cr_2O_3 phase. Fig. 7 shows that the peaks became sharper as a result of the increase in temperature. These results illustrated that the higher the temperature, the higher the crystallinity of the Cr_2O_3 was. Moreover, it also indicated an increase in the crystallite size. The crystallite size (D) is reported in Table 2. The crystallite size was calculated by the Scherrer formula [23]:

$$D=0.9\lambda/\Delta(2\theta)\cos\theta \qquad (7)$$

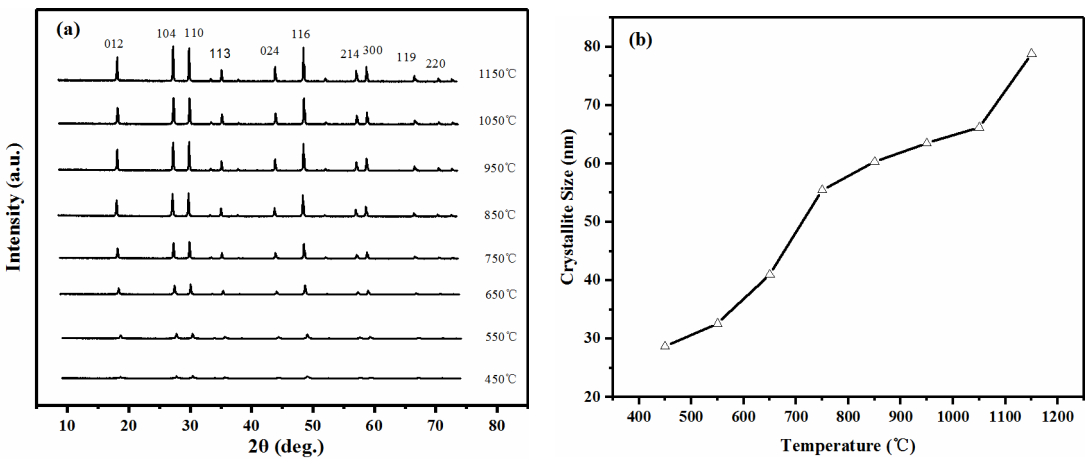

Figure 7. (a) XRD patterns and (b) crystallite size of Cr_2O_3 prepared by thermal decomposition of $(NH_4)_2CrO_4$ at 450 ℃, 550 ℃, 650 ℃, 750 ℃, 850 ℃, 950 ℃, 1050 ℃ and 1150 ℃.

Table 2. Comparison of particle size, crystallite size and specific surface area of Cr_2O_3

Temperature (℃)	Crystallites size (nm)	Average particle diameter (nm)	Specific surface area (m^2/g)
	XRD	SEM	
450	29	71	38.41
550	33	85	38.03
650	41	114	25.65
750	56	122	14.92
850	60	165	11.55
950	64	171	8.68
1050	66	187	7.26
1150	79	216	4.71

3.3.3. Fourier transform infrared (FTIR) spectroscopy

Fig. 8 shows the Fourier transform infrared spectroscopy of the samples. The IR intensity was accompanied by an increase in the temperature, which can be attributed to an increase in the particle size; this is also in agreement with the particle size results in Fig. 9. The vibration bands at 570 cm^{-1} and ~635 cm^{-1} are characteristic of the Cr_2O_3 structure [24]. Therefore, it can be concluded that the product was Cr_2O_3. The vibration at ~635 cm^{-1} appeared shifted towards the longer wavelength side with increasing temperature due to the reduction of oxygen defects with increasing grain size. On the other hand, the band at 1635 cm^{-1} and 3440 cm^{-1} was due to the bending and stretching of modes of water molecules, respectively [25]. Increasing the temperature reduced the intensity of the 3440 cm^{-1} band because of the decrease in the water content of Cr_2O_3.

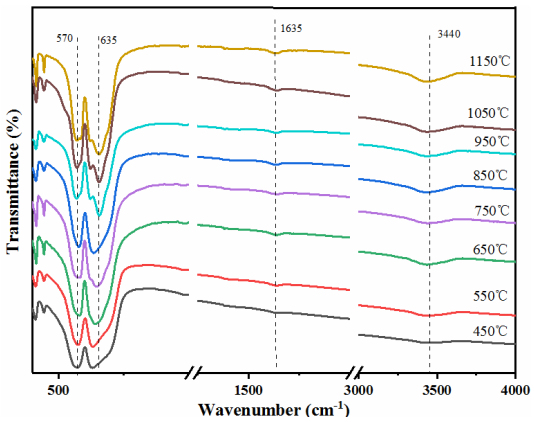

Figure 8. FTIR spectra for the indicated Cr_2O_3 samples prepared by thermal decomposition of $(NH_4)_2CrO_4$ at 450 °C, 550 °C, 650 °C, 750 °C, 850 °C, 950 °C, 1050 °C and 1150 °C.

3.3.4. Morphology analysis

Fig. 9 shows the morphology of the samples. The results revealed that the higher the temperature was, the larger the particle size. Increasing the temperature contributed to the thermal decomposition reaction of the ammonium chromate, so the particle size increased. Different thermal decomposition temperatures lead to different growth directions in the crystals, so the morphology changed. The effect of the thermal decomposition temperature on the particle size is consistent with that on the crystallinity. The particle size distribution of the Cr_2O_3 prepared at 450~650 ℃ was wide, ranging from 50 to 250 nm. There was an agglomeration phenomenon, and the particle morphology was irregular. A rough surface can be observed, especially for the large particles in Fig. 9 (a). The morphology of Cr_2O_3 prepared at 750~950 ℃ was approximately spherical. The particle size distribution was 50~300 nm. Furthermore, it can be observed in Fig. 9 (d)-(e) that there were streaks on the surface of the particles along the growth direction of the crystal face. When Cr_2O_3 was prepared at 1050~1150 ℃, the particle size distribution was 100~350 nm. The surface of the particles was very smooth, but they began to transform from spheres to short rods. The SEM images clearly showed the particle sizes, and the average particle diameter was determined by ImageJ [26] software, as shown in Table 2.

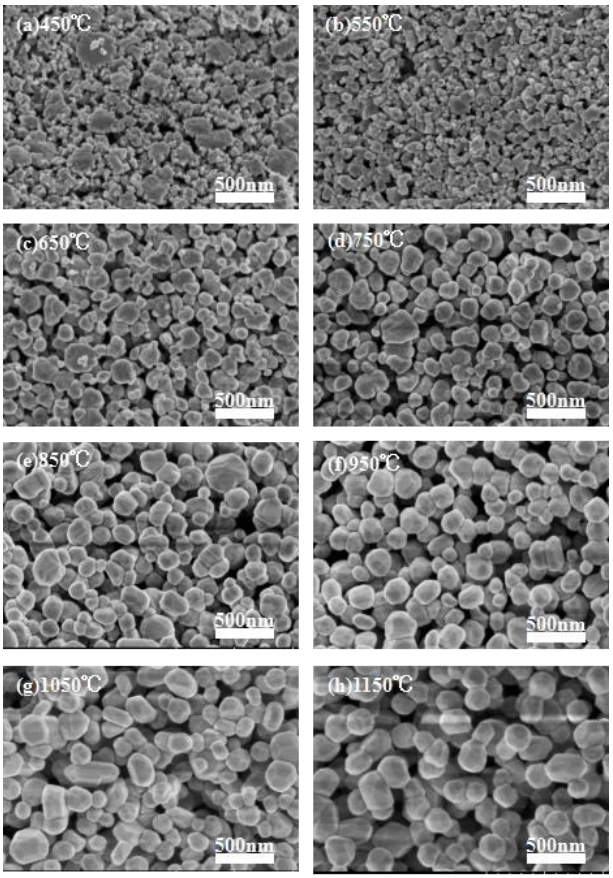

Figure 9. SEM photographs of Cr_2O_3 prepared by thermal decomposition of $(NH_4)_2CrO_4$ at (a) 450 ℃, (b) 550 ℃, (c) 650 ℃, (d) 750 ℃, (e) 850 ℃, (f) 950 ℃, (g) 1050 ℃ and (h) 1150 ℃.

3.3.5. Specific surface area and pore volume analysis

Fig. 10 shows the specific surface area and pore volume of the samples. The results revealed that the higher the temperature was, the smaller the specific surface area. Theoretically, an increase in the particle size decreases the specific surface area; the particle size results were also confirmed by SEM. The pore diameter of the products calcined under various temperatures was 3~38 nm. Therefore, the products were mesoporous materials. The specific surface areas of chromic oxide are listed in Table 2.

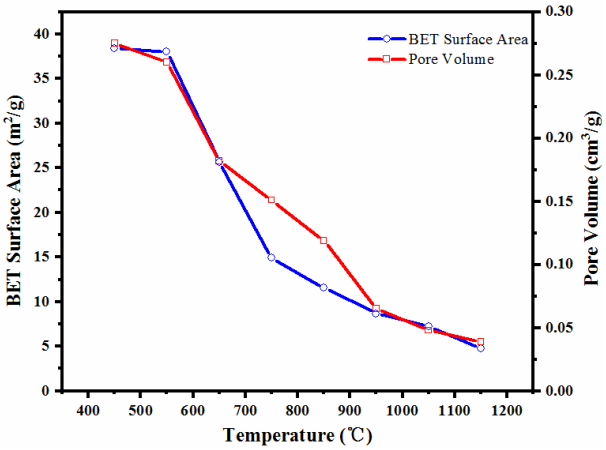

Figure 10. BET surface area and pore volume of Cr_2O_3 prepared by thermal decomposition of $(NH_4)_2CrO_4$ at 450 ℃, 550 ℃, 650 ℃, 750 ℃, 850 ℃, 950 ℃, 1050 ℃ and 1150 ℃.

3.3.6. Chroma analysis

Table 3. Chromatic coordinates of Cr_2O_3

T (℃)	L*	a*	b*	color
450	35.63	0.91	7.00	Dark-green
550	34.78	0.21	6.08	
650	41.43	-3.63	9.65	Pale-green
750	47.61	-9.34	14.28	
850	49.88	-10.34	15.34	Brilliant-green
950	49.97	-12.93	17.77	
1050	49.34	-14.02	17.88	
1150	48.16	-14.73	17.92	
S1	46.33	-15.14	19.87	

Table 3 shows the color parameters of the samples. The -a* b* values increased with increasing temperature. Chromium oxide with few crystal defects and complete crystallization had an improved color and bright color. [27]. However, the L* value did not increase with increasing temperature. This is due to the influence of the morphology of the chromium oxide on the dispersion, resulting in a decrease in the L* value. The sample calcined at 1150 ℃ already reached an a* value of -14.73, whereas the b* value of the commercial product was 15.14, which illustrated that the green tone of the sample was close to that of the commercial product. The L* values of the samples calcined over 750 ℃ were higher than that of the commercial product, which illustrated that the brightness of the sample was better than that of the commercial product. The b* values of the sample increased due to an increase in the temperature, but it was below the commercial product value so that the Cr_2O_3 looked yellowish. According to the L* a* b* results, the samples were bright green.

3.3.7. UV-vis analysis

Fig. 11 shows the UV–vis spectra of the samples. The spectra show that the band gap values were 1.91~2.25 eV and correspond to the absorption edges observed at 550~650 nm. Compared to the band gap value in the literature, i.e., 3.4 eV, the band Cr_2O_3 gap values were lower. The lower band gap values support the potential application as a catalyst. With an increase in the temperature, the band gap of the Cr_2O_3 increased in the absorption spectrum due to the particle size increase. Furthermore, the three absorption peaks of the products were due to the band gap transition of the Cr^{4+} ions (360 nm) and the electronic transitions of the Cr^{3+} ions (460 nm and 600 nm) [28].

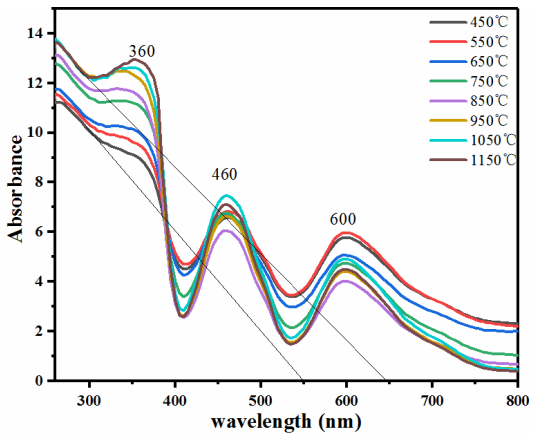

Figure 11. UV-vis absorption spectra of Cr_2O_3 samples prepared by thermal decomposition of $(NH_4)_2CrO_4$ at 450 ℃, 550 ℃, 650 ℃, 750 ℃, 850 ℃, 950 ℃, 1050 ℃ and 1150 ℃.

4. CONCLUSION

In this study, the preparation of Cr_2O_3 via electrooxidation and calcination represents a clean approach. The effect of current density, mole ratio of $NH_3{\cdot}H_2O$:$2CrO_4^{2-}$ and temperature on current

efficiency is discussed. When the current density was 140 A/m^2 and the molar ratio of $NH_3 \cdot H_2O$:2CrO_4^{2-} was 1:5, the current efficiency was 62% at room temperature, which illustrated that the green and efficient production of Cr was realized via electrooxidation. The TG-DTA results revealed that Cr_2O_3 with a purity of 99% was obtained with the reduction process of $Cr^{6+} \rightarrow Cr^{4+} \rightarrow Cr^{3+}$. Crystalline Cr_2O_3 with a fine particle size was confirmed by XRD and FTIR. The SEM and BET results showed Cr_2O_3 with an average particle size of 71~216 nm, and a specific surface area of 4~38 m^2/g was obtained. The UV-vis results revealed that the Cr_2O_3 with band gap values of 1.91~2.25 eV were a bright yellow-green color and may have good light catalyst properties.

ACKNOWLEDGEMENTS
Financial support from the General Program funding from Major Science and Technology Special Project in Qinghai Province of China (2016-GX-A10) and Qinghai Basic Research Project (2017-ZJ-786) are gratefully acknowledged.

References

1. G. Bai, H. Dai, Y. Liu, K. Ji, X. Li, S. Xie, *Catalysis Communications*, 36 (2013) 43.
2. J. Zhu, Y. Jiang, Z. Lu, C. Zhao, X. Li, L. Chen, J. Duan, *Journal of Colloid & Interface Science*, 498 (2017) 351.
3. J. L. Bobet, S. Desmoulins-Krawiec, E. Grigorova, F. Cansell, B. Chevalier, *Journal of Alloys & Compounds* 351 (2003) 217.
4. H. L. Zhang, S. T. Liang, M. T. Luo, M. G. Ma, P. P. Fan, H. B. Xu, P. Li, Y. Zhang, *Materials Letters*, 117 (2014) 244.
5. S. Khamlich, O. Nemraoui, N. Mongwaketsi, R. Mccrindle, N. Cingo, M. Maaza, *Physica B Condensed Matter*, 407 (2012) 1509.
6. [6] Y. Du, W. L. Cai, C. M. Mo, J. Chen, L. D. Zhang, X. G. Zhu, *Applied Physics Letters*, 74 (1999) 2951.
7. N. E. Fouad, *Journal of Thermal Analysis*, 46 (1996) 1271.
8. H. B. Xu, Y. Zhang, Z. H. Li, S. L. Zheng, Z. K. Wang, T. Qi, H. Q. Li, *Journal of Cleaner Production*, 14 (2006) 211.
9. B. Walawska, Z. Kowalski, *Journal of Cleaner Production*, 9 (2001) 219.
10. N. A. Dhas, A. Y. Koltypin, A. Gedanken, *Chemistry of Materials*, 9 (2011) 3159.
11. A. C. Santulli, M. Feygenson, F. E. Camino, M. C. Aronson, S. S. Wong, *Chemistry of Materials*, 23 (2011) 1000.
12. K. Anandan, V. Rajendran, *Materials Science in Semiconductor Processing*, 19 (2014) 136.
13. J. Su, H. Xue, M. Gu, H. Xia, F. Pan, *Ceramics International*, 40 (2014) 15051.
14. K. Anandan, V. Rajendran, *Materials Letters,* 146 (2015) 99.
15. C. A. C. Sequeira, D. M. F. Santos, *Journal of the Brazilian Chemical Society*, 20 (2009) 387.
16. C. Innocent, P. Huguet, J. L. Bribes, G. Pourcelly, M. Kameche, *Physical Chemistry Chemical Physics*, 3 (2018) 1481.
17. P. Zuman, *Microchemical journal*, 72 (2001) 231.
18. A. J. Bard, L. R. Faulkner, *Journal of Chemical Education*, 60 (2001) 669.
19. Y. Fan, X. Wang, M. Wang, *Hydrometallurgy*, 136 (2013) 31.
20. X. Wang, H. Wang, D. Gao, B. Chen, Y. Meng, M. Wang, *Hydrometallurgy*, 177 (2018) 94.
21. A. K. Galwey, L. Poeppl, S. Rajam, *Cheminform*. 14 (1983) 2143.
22. S. Rajam, A. K. Galwey, *Journal of the Chemical Society Faraday Transactions*, 78 (1982) 2553.

23. S. Khamlich, E. Manikandan, B. D. Ngom, J. Sithole, O. Nemraoui, I. Zorkani, R. Mccrindle, N. Cingo, M. Maaza, *Journal of Physics & Chemistry of Solids*, 72 (2011) 714.
24. C. W. Li, T. Qi, F. Wang, Y. Zhang, Z. H. Yu, *Chemical Engineering & Technology*. 29 (2006) 481.
25. Z. M. Yao, Z. H. Li, Y. Zhang, *Journal of Colloid & Interface Science*, 266 (2003) 382.
26. Z. Pei, X. Zhang, *Materials Letters*, 159 (2015) 357.
27. E. W. A. Young, J. H. Gerretsen, J. H. W. D. Wit, *Cheminform*, 18 (1987) 2257.
28. L. D. Zhang, C. M. Mo, W. L. Cai, G. Chen, *Nanostructured Materials*, 9 (1997) 563.

© 2019 The Authors. Published by ESG (www.electrochemsci.org). This article is an open access article distributed under the terms and conditions of the Creative Commons Attribution license (http://creativecommons.org/licenses/by/4.0/).